AGU ADVANCING EARTH AND SPACE SCIENCES

Water Resources Research

RESEARCH ARTICLE

10.1029/2025WR040035

In Situ Study of Coupled Mineral Dissolution and Precipitation Processes With Gas Production in Porous Media Using Magnetic Resonance Imaging

Lara Wegner[1], Andreas Pohlmeier[2], Yumeng Wang[1], Martina Klinkenberg[1], Dirk Bosbach[1], and Jenna Poonoosamy[1]

[1]Institute of Fusion Energy and Nuclear Waste Management (IFN-2), Forschungszentrum Jülich GmbH, Jülich, Germany, [2]Institute of Bio- and Geosciences (IBG-3), Forschungszentrum Jülich GmbH, Jülich, Germany

Key Points:

- Development of an experiment enabling live monitoring of coupled processes with gas production using magnetic resonance imaging
- Gas bubbles trapped by newly formed precipitates contribute to porosity clogging
- Provision of data sets on coupled processes with gas production for testing conceptual models in reactive transport codes

Supporting Information:

Supporting Information may be found in the online version of this article.

Correspondence to:

L. Wegner,
l.wegner@fz-juelich.de

Citation:

Wegner, L., Pohlmeier, A., Wang, Y., Klinkenberg, M., Bosbach, D., & Poonoosamy, J. (2025). In situ study of coupled mineral dissolution and precipitation processes with gas production in porous media using magnetic resonance imaging. *Water Resources Research*, *61*, e2025WR040035. https://doi.org/10.1029/2025WR040035

Received 21 JAN 2025
Accepted 25 JUN 2025

Author Contributions:

Conceptualization: Lara Wegner, Jenna Poonoosamy
Data curation: Lara Wegner
Formal analysis: Lara Wegner, Andreas Pohlmeier, Jenna Poonoosamy
Investigation: Lara Wegner, Andreas Pohlmeier, Martina Klinkenberg
Methodology: Lara Wegner, Yumeng Wang, Jenna Poonoosamy
Visualization: Lara Wegner
Writing – original draft: Lara Wegner, Yumeng Wang, Jenna Poonoosamy
Writing – review & editing: Lara Wegner, Andreas Pohlmeier, Yumeng Wang, Martina Klinkenberg, Dirk Bosbach, Jenna Poonoosamy

Abstract Coupled mineral dissolution, precipitation, and gas exsolution (CDPG) are critical processes in subsurface energy applications. These phenomena occur during natural hydrogen degassing from serpentinized mafic rocks, anoxic corrosion of metallic nuclear waste canisters, and CO_2 sequestration in deep saline aquifers. However, the behavior of exsolved gas within rock matrices remains poorly understood, particularly whether it is trapped by precipitates contributing to porosity clogging, or migrates with fluid flow and dissolves downstream. These uncertainties limit the accuracy of reactive transport models for predicting the long-term evolution of such systems. Here, we developed a 3D reactive transport experiment to study the coupled dissolution of witherite ($BaCO_3$), precipitation of barite ($BaSO_4$), and exsolution of CO_2. Magnetic resonance imaging (MRI) was used for live monitoring of heterogeneous gas production and transport, to quantify the relative gas content across the porous medium. In situ measurements of pH, pCO_2, differential pressure, and effluent ion concentrations aligned with MRI findings that the dissolution-precipitation process and gas exsolution lasted for 25 hr. Scanning electron microscopy showed porosity reduction resulted from barite precipitation in pore spaces and localized clogging from precipitation on CO_2 bubble surfaces. Mineral dissolution is best modeled with a reactive surface area approach that accounts for mineral passivation. While permeability changes can be estimated using the Van Genuchten-Mualem equation based on MRI-measured water saturation in inert porous media, this method fails to account for changes in pore structures with mineral precipitation. These results provide a robust data set for benchmarking reactive transport models and advancing understanding of CDPG.

Plain Language Summary Gas plays an important role in natural and engineered subsurface processes, such as during natural hydrogen gas production and during metal canister corrosion. It can also occur as a byproduct of mineral dissolution and precipitation reactions. However, the flow and transport behavior of the produced gas in porous rocks is still poorly understood. The main question is, whether it can be trapped in the pore space and consequently clog the system or whether the gas moves with the liquid and then dissolves. To help answer these questions, we developed a 3D reactive transport experiment to investigate the coupled dissolution of witherite, precipitation of barite, with the production of CO_2 during the reaction in a pore space. We conducted a live monitoring of the gas production and distribution using magnetic resonance imaging. Additionally, we measured several parameters to estimate how the system chemically changes during the reaction, and observed microscopic structural changes of pores. It shows that precipitation in the pore space and especially on the surface of CO_2 gas bubbles clogs the system. These results can be used as an experimental benchmark to set up and improve models by helping to understand the complexity of coupled underground processes.

1. Introduction

Coupled mineral dissolution and precipitation is characterized by the dissolution of a primary mineral and the concurrent precipitation of a secondary mineral. This process often releases gases as a byproduct of primary mineral dissolution. For instance, hydrogen can be generated naturally during the serpentinization of ultramafic rocks (Lefeuvre et al., 2022; Osselin, Soulaine, et al., 2022) or during anoxic corrosion of metallic waste canisters in deep geological repositories for radioactive waste (El Mendili et al., 2015; Vehling & Shao, 2023). In both cases, the oxidation reaction can be described by the Schikorr reaction. It refers to the transformation of $Fe(OH)_2$ to magnetite, during serpentinization the Fe in Fe-silicates is oxidized, the source of H_2 is water as an oxidant.

Similarly, gas exsolution can occur during CO_2 sequestration in deep saline aquifers (R. Xu et al., 2017) and sandstone (Krevor et al., 2011). The formation of secondary minerals plays a critical role in subsurface geochemistry, as these phases can either induce porosity and fracturing within the rock matrix, promote fluid movement and enhance primary mineral replacement, or alternatively, form protective layers that inhibit further primary mineral dissolution (C. V. Putnis & Putnis, 2022). However, the fate of gas generated during these reactions remains unclear, specifically whether it becomes entrapped within precipitated secondary minerals or is transported by the surrounding fluid.

Coupled mineral dissolution and precipitation has non-linear effects on the rock permeability (Beckingham, 2017; Jiang & Tsuji, 2014; Kang et al., 2003; Osselin, Pichavant, et al., 2022; Poonoosamy, Klinkenberg, et al., 2020; Steinwinder & Beckingham, 2019; Yang et al., 2024) and diffusivity (Chagneau et al., 2015; Emmanuel & Berkowitz, 2005; Lönartz et al., 2023; Poonoosamy et al., 2022; Rajyaguru et al., 2019; Schulz, 2020; Schulz et al., 2017), and can significantly impact the effectiveness of subsurface storage and extraction systems. Trapped gases in secondary mineral phases can compromise the reliability of energy-related subsurface applications, such as acidic stimulation during hydraulic fracturing, CO_2 sequestration, and deep geological repositories for radioactive waste. As a result, the sustainable use and structural integrity of these subsurface systems rely on the development of predictive models that accurately capture the evolution of hydrogeochemical processes with fluid flow and gas generation (multi-phase flow), as well as the transport of contaminants and radionuclides under dynamic subsurface conditions.

A comprehensive understanding of the factors that regulate the coupled mineral dissolution and precipitation, gas exsolution (CDPG), and the latter's transport or entrapment is critical for the development of mechanistic models for implementation in reactive transport models (Steefel, 2019). However, understanding gas-water-rock interactions and their impact on the transport properties of porous media is difficult due to the complexity and non-linear behavior of multiple simultaneous processes. Natural and technical materials, such as rock matrices or concrete with varying mineral composition and pore sizes, often provide only phenomenological insights. To gain a detailed mechanistic understanding, simplified "model systems" are employed, allowing isolated processes to be studied under controlled chemical and hydraulic conditions. Such experiments based on "model systems" have been proposed for the investigation of mixing induced precipitation (Katz et al., 2011; Tartakovsky et al., 2007, 2008), porosity clogging (Chagneau, 2015; Jenni et al., 2024; Lönartz et al., 2023; Rajyaguru et al., 2019), and transport in partially saturated porous media (Ahmadi et al., 2022; Muniruzzaman et al., 2014). For instance, Poonoosamy et al. (2015) studied coupled mineral dissolution of a primary mineral (celestine) and precipitation of a secondary mineral (barite) in fully saturated porous media to validate key concepts in pore-scale reactive transport modeling (RTM) (Poonoosamy, Wanner, et al., 2021). Further experiments addressed nucleation in confined spaces (Poonoosamy et al., 2016), mineral passivation mechanisms and their effects on mineral reactivity, as well as the impact of precipitation mechanisms on pore connectivity, localized porosity clogging (Poonoosamy, Haber-Pohlmeier et al., 2020), and consequently, the permeability of porous media (Poonoosamy, Klinkenberg et al., 2020). These findings initiated the integration of classical nucleation theory into pore-scale reactive transport models (Deng et al., 2022; Prasianakis et al., 2017) to explore nucleation processes in porous media, fostering further developments in continuum scale reactive transport models (Boampong et al., 2024; Li et al., 2017; Poonoosamy, Mahrous, et al., 2021; Steefel & Hu, 2022; Steefel & Yang, 2021).

Experiments dedicated to study mineralogical reactions in variably saturated porous media remain limited and typically focused on biogeochemical reactions (Haberer et al., 2015) or only on dissolution processes involving gas production within microfluidic devices (Soulaine et al., 2018; Zhou et al., 2023). Soulaine et al. (2018) investigated the fate of gas produced during mineral dissolution by simulating the dissolution of a calcite array representing a homogeneous reactive porous medium. While single-phase flow promoted wormhole formation, gas-phase presence created clusters that hindered acid distribution, reduced dissolution rates, and suppressed wormhole development. The numerical investigations were, however, never validated by experimental observations.

In this study, we introduce a novel 3D-reactive transport experiment featuring simplified chemistry, dynamically monitored through time-resolved Nuclear Magnetic Resonance Imaging (MRI), offering new insights into complex subsurface processes. Coupled dissolution and precipitation is based on the precipitation of Ba with dissolved SO_4^{2-} as $BaSO_4$ (barite) from dissolving $BaCO_3$ (witherite). The experiment is conducted under controlled conditions and the set-up allows in situ measurements of the differential pressure, partial pressure of

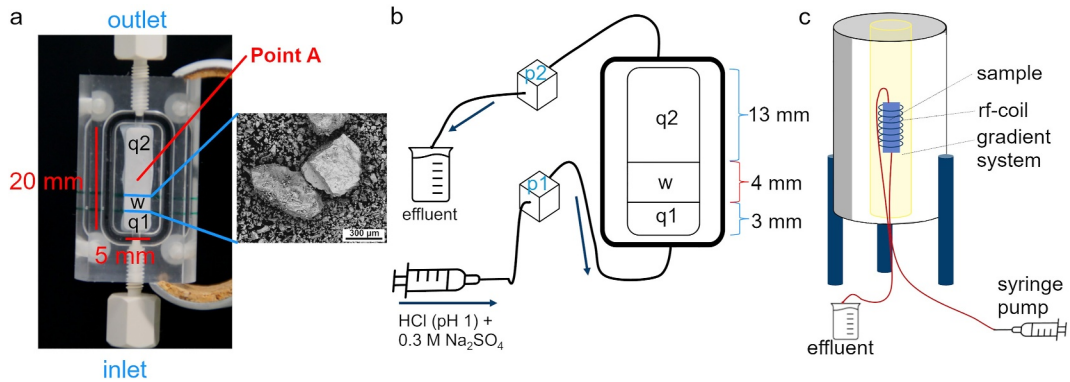

Figure 1. Experimental set-up. (a) Picture of the flow through reactor filled with a homogeneous mixture of large and small $BaCO_3$-crystals (w) sandwiched between two layers of quartz sand (q1 and q2). The inlet (bottom) and outlet (top) are indicated and point A (1 cm from inlet) indicates sampling spot for the measurement of pCO_2 and pH. (b) Schematic experimental set-up. Reactor is filled with three layers. p1 and p2 are pressure sensors to measure differential pressure. (c) The reactor is placed in the magnetic resonance imaging-scanner, inside the rf-coil and the reaction is monitored continuously over a period of 48 hr.

CO_2 (pCO_2), pH, and effluent control of aqueous anion and cation concentrations. MRI allows a non-invasive live monitoring of the gas production and evolution in the system with time. Post-experimental micro-structural analyses were performed on the reacted porous medium using Raman, scanning electron microscopy (SEM), and energy dispersive X-ray spectroscopy (EDS) to monitor the spatial distribution of gas and precipitate in the reacted material. This work explores the fate of gas during CDPG and presents a scientific basis for identifying the challenges of multi-phase RTM and experimental data sets for benchmarking in future studies.

2. Experimental Methods

2.1. Experimental Set-Up

The experimental set-up consists of a plexiglas micro-reactor with a reaction space with the dimensions $20 \times 5 \times 5$ mm (length × width × depth) (Figure 1a). It is a custom design to fit into the radio-frequency-coil used in the nuclear magnetic resonance (NMR) scanner with an inner diameter of 2.5 cm (Figure 1c). The reactor was filled with a layer of quartz sand (q1, 3 mm), followed by a layer of the reactive material (w, 4 mm), natural witherite, and lastly a second layer of quartz sand (q2, 13 mm) (Figure 1b, for details of experimental set-up see Text S2 in Supporting Information S1). The q1-layer enables uniform flow, mitigating fingering of reactive solution into the w-layer.

The quartz sand used is a commercial acid-washed silicon dioxide with a grain size of 0.1–0.3 mm and a purity of 99.9%. The initial porosity ϕ of q1 and q2 was determined at 0.39 ± 0.1. The reactive layer consisted of a crushed and dry sieved natural occurring witherite crystal with low porosity. The raw crystal is mainly composed of $BaCO_3$ (87.1%), $CaCO_3$ (10.4%), and $SrCO_3$ (2.5%) (see Text S1 in Supporting Information S1 for the characterization of witherite). The layer consisted of a mixture of small grains (30 wt.%, 20–63 µm) and larger grains (70 wt.%, 250–400 µm) to maintain mechanical stability of the w-layer during the dissolution process. The layer was compacted to a porosity of 0.29 ± 0.1. The inlet and outlet of the reactor were covered with a fine mesh synthetic filter with high permeability to prevent sand grains from clogging the tubing. A solution consisting of hydrochloric acid (HCl) at pH 1 and 0.3 M Na_2SO_4 was injected at a constant flow rate of 2 µL min^{-1} (3.33×10^{-11} m^3 s^{-1}) corresponding to a Darcy flow velocity of 1.33 µm s^{-1} for 48 hr. A Legato 200 syringe pump (kd Scientific, Harvard Apparatus, Holliston, MA, USA) equipped with a Hamilton 5 mL glass syringe was used for injection. The Péclet number, which quantifies the relative significance of advective versus diffusive transport (Reynolds, 1883), was calculated for the q1, w, and q2-layers at the initial stage as 10.0, 13.7, and 44.4, respectively (Table 1). This calculation was based on the effective diffusion coefficient of Na^+ in water at 298.15 K (Robinson & Stokes, 2002) and used the length of each individual layer as the characteristic length (Table 1, see Text S2 in Supporting Information S1 for details). The Péclet numbers >1 imply predominantly

Table 1
Initial (t = 0 hr) and Final (t = 48 hr) Experimental Parameters

Experimental parameter	$t = 0$ hr	$t = 48$ hr
Flow rate ($m^3\ s^{-1}$)	3.33×10^{-11}	3.33×10^{-11}
Na_2SO_4 (mol L^{-1})	0.3	0.3
pH (–)	1	1
(H^+) (10^{-pH})	0.1	0.1
Temperature (°C)	21	21
Length q1 (mm)	3	–
Length w (mm)	4	–
Length q2 (mm)	13	–
Absolute permeability (total) k_{tot} (m^2)	6.97×10^{-14}	6.03×10^{-15}
Permeability sand layer 1 k_{q1} (m^2)	2.89×10^{-12}[a]	6.80×10^{-13}[b]
Permeability sand layer 2 k_{q2} (m^2)	2.89×10^{-12}[a]	4.90×10^{-13}[b]
Permeability witherite layer k_w (m^2)	1.07×10^{-14}	Not determined
Porosity ϕ (–) q1 and q2	0.39	–
Porosity ϕ (–) w	0.29	–
Péclet number (Pe) (–) q1	10.0	–
Pe (–) w	13.7	–
Pe (–) q2	44.4	–

[a]Falling head method. [b]Van Genuchten-Mualem.

advective solute transport in all layers. The geochemical reactions expected in the w-layer are based on the following chemical equations:

$$\begin{gathered} BaCO_{3(s)} + 2H^+_{(aq)} \rightleftharpoons Ba^{2+}_{(aq)} + H_2O_{(l)} + CO_{2(aq)} \\ Ba^{2+}_{(aq)} + SO^{2-}_{4(aq)} \rightleftharpoons BaSO_{4(s)} \\ CO_{2(aq)} \rightleftharpoons CO_{2(g)} \end{gathered} \tag{1}$$

The injection of the acid solution is expected to induce the dissolution of $BaCO_3$ and the dissolved Ba^{2+} reacts with the injected $SO^{2-}_{4(aq)}$ to produce $BaSO_4$ (see Equation 1). In addition to witherite, the strontianite and calcite present in the system are also expected to dissolve. However, the precipitation of celestine and gypsum is unlikely due to their higher solubility product when compared to barite (see Table 2) and the limited availability of the necessary cations for their respective phases to form. The experiment was conducted five times in total with all experiments following the same experimental set-up. Two experiments were performed inside the MRI scanner to monitor and quantify gas production and transport and water content. Three additional experiments were conducted (outside the MRI scanner) to test reproducibility, collecting effluent, and measuring pH, pCO_2, and differential pressure.

Differential pressure was monitored with two pressure sensors recording inlet and outlet pressure (MPS-V2-S-0, Elveflow, Elvesys Group, Paris, France). Measurements were used to evaluate the initial absolute permeability of the system and to provide an indication of the changes in the transport properties of the porous medium during the experiments. The sand regions had an initial effective permeability of 2.89×10^{-12} m^2 (determined by falling head method, for details see Text S2 in Supporting Information S1) and the $BaCO_3$ layer had an initial effective permeability of 1.07×10^{-14} m^2 (details of the calculation see Text S2 in Supporting Information S1). The differential pressure is used as a relative value to emphasize the change of the differential pressure in the system during the experiment with time (calculation of relative value see Text S2 and Equation S10 in Supporting Information S1). Methylthymol blue served as both a tracer and pH indicator, allowing for the monitoring of changes in flow pathways and the visual assessment of pH fluctuations in the system. Partial pressure of CO_2 was measured in situ with photoluminescent sensor spots (CO_2-1 SMA, PreSens Precision Sensing GmbH, Regensburg, Germany) integrated into the center of the reacting space located in the q2-layer (Figure 1a). The PreSens pCO_2 sensor determines the concentration of dissolved CO_2 in liquid using photoluminescence. At the same time, it continuously measures ambient pressure. Using these values, the sensor applies Henry's Law to calculate and output the partial pressure of CO_2 (pCO_2) in hPa. The initial experimental conditions are summarized in Table 1; for details refer to Text S2 in Supporting Information S1.

Table 2
Solubility Products of Minerals Used and Possible Precipitation Products and Dissolution Rate Constants

Mineral	Solubility product K^0_{sp}	Dissolution rate constant k_r[mol m^{-2} s^{-1}]
Witherite ($BaCO_3$)	$10^{-8.56}$[a]	$10^{-4.12}$[a]
Calcite ($CaCO_3$)	$10^{-8.48}$[a]	$10^{-4.05}$[a]
Strontianite ($SrCO_3$)	$10^{-9.27}$[b]	$10^{-4.05}$[c]
Barite ($BaSO_4$)	$10^{-9.96}$[d]	–
Anhydrite ($CaSO_4$)	$10^{-4.21}$[d]	–
Gypsum ($CaSO_4 * 2H_2O$)	$10^{-4.59}$[d]	–
Celestine ($SrSO_4$)	$10^{-6.58}$[d]	–

[a]Chou et al. (1989). [b]Plummer and Busenberg (1987). [c]Oelkers and Addassi (2025). [d]Hummel and Thoenen (2021).

The effluent was sampled every hour. Anions (Cl^- and SO_4^{2-}) were analyzed with ion exchange chromatography (IC) and inductively coupled plasma-optical emission spectrometry was used to analyze cations (Ba^{2+}, Sr^{2+}, Ca^{2+}, and Na^+). Table S3 reports effluent concentrations with time.

2.2. Magnetic Resonance Imaging Sequences

Magnetic resonance imaging allows for a non-invasive live monitoring of the gas production and evolution in the system with time. Additionally, analysis of the NMR signal with regards to the relaxation behavior has been used to monitor the water content (see Text S4 in Supporting Information S1 for a detailed description of MRI data processing). NMR was performed with a Bruker vertical super wide bore 4.7 T MRI magnet (Bruker Biospin GmbH, Rheinstetten, Germany). Additionally, the scanner is equipped with a Micro 2.5 gradient system and a radio frequency (rf) coil with an inner diameter of 2.5 cm. The system is operated by a Bruker Avance III console (Bruker Biospin GmbH, Rheinstetten, Germany) and Paravision 6 software (Bruker Biospin GmbH, Rheinstetten, Germany). The syringe pump was placed outside the stray field of the magnet to ensure that the pump worked properly (Figure 1c).

A multi-slice spin echo (Bruker: MSME with one echo recorded) method with a field of view of 1 cm × 2.2 cm (96 × 192 pixel image resolution) was used to monitor the reaction for 42 hr. The sequence was repeated every 30 min. The echo time was set at $t_E = 3$ ms with a repetition time of 4,000 ms over two averages and one repetition. A coronal oriented slice package of 9 slices with 0.6 mm thickness and a slice gap of 0.1 mm was used for imaging. The quantification of the gas content in the pore space over time was achieved through image segmentation, as the produced gas locally decreased pixel intensity compared to water-filled pores (see Text S4 in Supporting Information S1 for details). With the MSME sequence it is not possible to monitor the gas production in the w-layer, due to the short T_2 (transverse relaxation) in relation to echo time. The obtained relative gas content is used to evaluate the water content Θ across the q1 and q2-layer with the following equation:

$$\Theta = 1 - \textit{relative gas content} \tag{2}$$

Furthermore, the water content enables analysis of the effective saturation S_e of the porous medium. It is calculated by:

$$S_e = \frac{\Theta - \Theta_r}{\phi - \Theta_r} \tag{3}$$

where Θ_r is the residual water content and ϕ is the porosity. For details of the calculations and experimental determination of Θ_r refer to Text S2 in Supporting Information S1.

For comparison, the water content was additionally mapped by a slice selective ultra-short TE sequence (Bruker: UTE) (Fabich et al., 2016; Robson et al., 2003) with a field of view of 2.5 cm × 2.5 cm. A coronal oriented slice package with 5 slices with 1 mm thickness and a slice gap of 0.5 mm was used for this sequence. A thin capillary with 32% H_2O and 68% D_2O, and 4 mmol L^{-1} $CuSO_4$ for relaxation acceleration was used as a reference value for a pure water phase. The sequence was repeated every hour. The UTE sequence was used to cross-check water content mapping by the MSME sequence. In this experimental set up, the pore space is either filled with gas or with a liquid phase, and therefore the two data sets can be used complimentary. The MSME sequence is inherently prone to signal loss due to rapid T_2 relaxation. Instead, UTE monitors the T_2* decay, which is faster, but since no time is needed for generation and monitoring spin echoes, acquisition is much faster (Robson et al., 2003) and thus, water content mapping is possible in porous media. However, it has lower resolution than the MSME sequence (see Text S4 in Supporting Information S1 for details).

Image segmentation and image processing was performed with Fiji (Image J 1.54f, Wayne Rasband and contributors, National Institutes of Health, Bethesda, MD, USA) and exponential fitting of the processed data was done with Origin (OriginLab Corporation, Northampton, MA, USA). Scans are colored with a yellow to dark blue look up table according to pixel intensity. The contrast of the scans is influenced by the liquid content of the system and the properties of the materials used, such as magnetic susceptibility. Consequently, the water-filled pores in the saturated quartz sand layers exhibit higher pixel intensity compared to those of the w-layer, which

relaxes rapidly due to the inherent material properties of the witherite mineral. A detailed description of the data processing of all NMR and MRI data is given in the Text S4 in Supporting Information S1.

2.3. Post-Experimental Micro-Structural Analysis

For post-experimental analysis, two reactors (from the five experiments) were flushed with one pore volume of high purity water to remove the reacted pore solution. The flow through reactors were then carefully opened and dried at 50°C in a drying cabinet for 24 hr.

After drying, the quartz sand was removed from one of the reactors, allowing the cemented $BaCO_3$ part to be extracted as a single, intact piece. Raman mapping was performed in the reacted material using an automated inverted microscope (WITec alpha300 Ri Inverted Confocal Raman Microscope, WITec Wissenschaftliche Instrumente und Technologie GmbH, Ulm, Germany). The machine is equipped with a Nd: YAG laser with an excitation wavelength of $\lambda = 532.236$ nm, a thermoelectrically cooled CCD Camera, and an ultra-high-throughput spectrometer (UHTS300S). The laser power was set at 28 mW, and mapping was performed with a 100× oil immersion objective from Nikon. The Raman map was recorded from an area of 100 μm width, 140 μm height (200 × 280 pixels), and 10 μm depth at a randomly chosen location inside the reacted sample. Raman images were processed with WITec Project FIVE (WITec, WITec Wissenschaftliche Instrumente und Technologie GmbH, Ulm, Germany) and processed image stacks were combined with the Fiji 3D viewer. The second dried sample was further prepared for SEM analysis. To stabilize and preserve the sample, it was impregnated under vacuum with a two-component clear epoxy resin (Araldite 2020 A + B, Huntsman Advanced Materials, Switzerland). The applied vacuum effectively removed all loose particles from the reaction space, leaving only the cemented material intact. The reacted sample was cut longitudinally through the middle, and then polished. Micro-structural changes in the w-layer were investigated with a FEI Quanta 200F electron microscope (Thermo Fisher Scientific, Waltham, MA, USA) equipped with EDS (Octane elect PLUS silicon Drift Detector, EDAX, AMETEK GmbH, Weiterstadt, Germany) in low vacuum mode (60 Pa) at an accelerating voltage of 20 kV and a working distance of 10 mm. Elemental mappings (Ba(L) and Sr(L) lines, Ca(K), C(K), O(K), Si(K), Sr(K), and S(K) lines) were conducted at different locations in the reacted layer to visualize the distribution of the original carbonate material and precipitated sulfates. Maps were recorded at a magnification of 400× and 1,000×, with a resolution of 512 × 400 pixels.

3. Results

3.1. Gas Production and Relative Gas Content From Nuclear Magnetic Resonance Measurements

Figure 2a shows the representative results of the third slice of the slice package of the MRI measurements, visualizing gas production during the reaction. As described in Text S2 in Supporting Information S1, the system was set up to be initially fully saturated with ultra pure water, so gas being produced through the chemical reaction locally decreases the pixel intensity. However, low intensity pixels were observed on the left side of the cell already in the first scan (Figure 2a) as a result of trapped gas during the packing. Nevertheless, we can assume that the system is fully saturated for the presented work here.

After 8 hr (i.e., two pore volume exchanges of the complete sample) enough gas was produced that it became visible in the scans. The gas propagated upwards, forming distinct gas streams that originated in the w-layer moving toward the outlet of the system, where the gas accumulated. This can be observed in the Movie S1 included in the online version of the Supporting Information S1 showing the complete time lapse of the gas production captured with MRI. During the first 8 hr gas is also pushed into the q1-layer, most likely due to gas generation at the interface of the q1 and w-layer, but here spreading uniformly. The movement of gas toward the inlet can be explained by the relatively low solution injection rate used in our experiments. After 25 hr the gas content visually did not increase further. Although it cannot be assumed that gas production ceased entirely, the MRI scans no longer captured any additional gas accumulation. Instead, the gas became trapped in the pore space, and the porous medium did not re-saturate despite continuous injection of the reacting solution. The pixel intensity in the $BaCO_3$ layer is roughly constant with time. These observations highlight the complexity of multiphase flows with flow rates controlling the water-gas distribution patterns in the porous media (Soulaine et al., 2018).

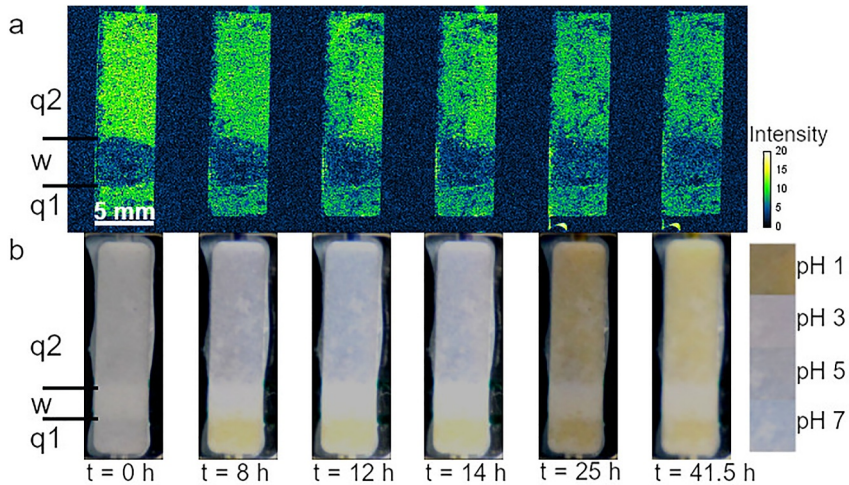

Figure 2. Magnetic resonance imaging scans and photos of pH indicator during the experiment. (a) Visualized gas production in the flow through reactor with time at $t = 0$, 8, 12, 14, 25, and 41.5 hr. The color table refers to voxel intensity of the spin echo for $t_E = 3$ ms in arbitrary units. Field of view: 1.6×2.2 cm, matrix size 96×192. Shown is one central vertical slice of 0.6 mm thickness. Gas phase in q1 and q2 compartments manifests by low intensity due to short t_E and lower water content. $t = 0$ hr: initial fully saturated state, $t = 8$ hr: enough gas has accumulated that it becomes visible in the scans, $t = 12$ and 14 hr: accumulation of gas in the pore space of q1 and q2, $t = 25$ hr: visually no more gas is being produced after 25 hr, $t = 41.5$ hr: final scan. (b) Series of photographs depicting time lapse of injection with pH indicator methylthymol blue visualized in the q1 and q2 region. $t = 0$ hr: initial state of the experiment. The pore space is saturated with ultra pure water and the injection with the acidic solution was just started. The pH value in the q1-layer constantly stays at pH 1. The change of pH in the q2-layer: $t = 8$ hr: pH 6, $t = 12$ hr: pH 7, $t = 14$ hr: pH 6, $t = 25$ hr: pH 1, $t = 41.5$ hr: pH 1.

In the q1 and q2-layer (Figure 3a), the gas content was quantified as relative gas content (volume fraction of gas) directly from the MSME scans as described in the Text S4 in Supporting Information S1. The temporal development is depicted in Figure 3a. In the w-layer (Figure 3b) this was not possible due to the fast T_2 relaxation and lower water content. Therefore, we used the UTE sequence and calculated the relative gas content from the change in water content as described in detail in Text S4 in Supporting Information S1. The relative gas content in the q1-layer (Figure 3a, black dots) initially increased, exceeding 0.2 within the first 3 hr, before decreasing over the next 20 hr. This trend suggests that the layer was not fully saturated during this period. Subsequently, the gas content begins to rise again, reaching a final value of 0.09. The observed secondary increase in gas content, despite the presumed completion of the reaction, may be explained by gas re-entering the q1-layer from the w-layer. The low thickness of the q1-layer (3 mm) also means that the relative gas content is only averaged over a small area, compared to the q2-layer. Additionally, boundary effects from the reactor walls may impact results further.

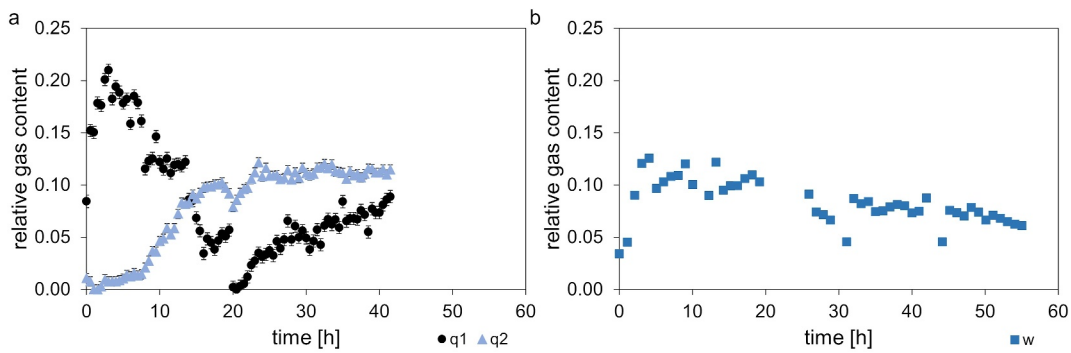

Figure 3. Summary of results gathered from magnetic resonance imaging scans and nuclear magnetic resonance data. (a) Relative gas content of q1 and q2-layers determined from MSME sequence. (b) Relative gas content of w-layer determined from relative water content measured with UTE sequence (see Text S4 in Supporting Information S1 for details).

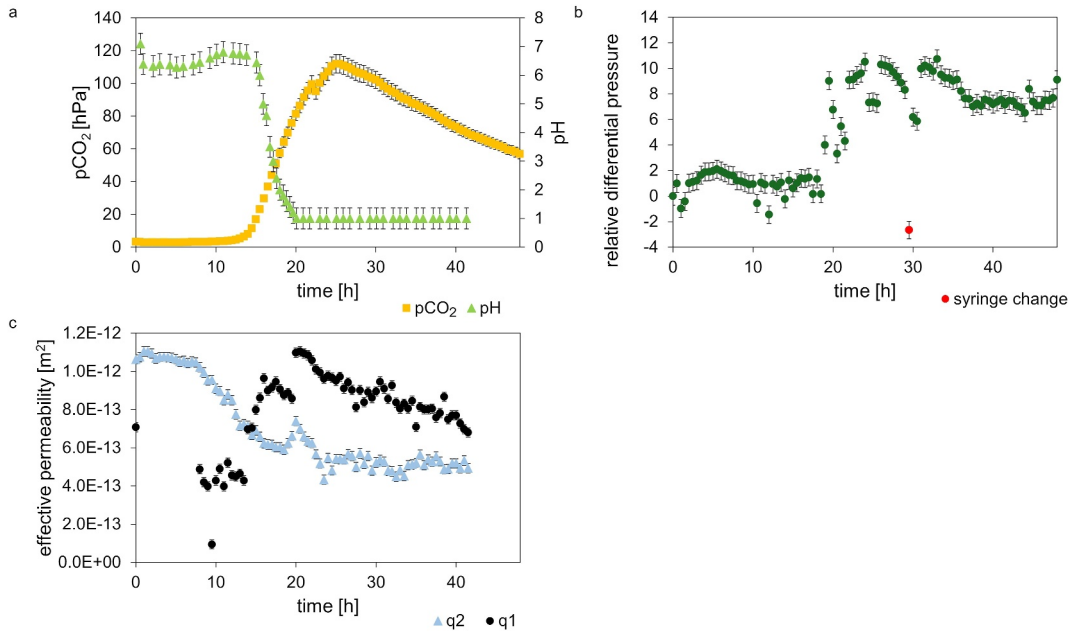

Figure 4. (a) In situ measurements of partial pressure of CO_2 (hPa) and pH recorded in the q2-layer, indicated by point A in Figure 1a. (b) Relative differential pressure monitored between inlet and outlet pressure with two microfluidic pressure sensors. Marked in red is the change of syringe during injection. (c) Estimated effective permeability changes determined by the Van Genuchten-Mualem equation with time in the q1 and q2-layer.

In the w-layer (Figure 3b, blue squares), the relative gas content increases rapidly over the first 4 hr, peaking at 0.12, stays fairly constant until 25 hr have passed and then decreases gradually to reach a final value of 0.06 after 55 hr. This also supports the hypothesis that the main reaction is taking place during the first 25 hr. The relative gas content in the q2-layer (Figure 3a, blue triangles), remains consistently low at approximately 0.02 for the first 8 hours. Subsequently, it increases rapidly, reaching a maximum value of 0.12 after 25 hr. This trend indicates that the primary reaction occurs within the initial 25 hr, after which gas production either slows significantly or ceases altogether. These observations are corroborated by MRI scans (Figure 2a), which also demonstrate gas exsolution over the 25-hr period. Furthermore, this behavior aligns closely with trends in pCO_2 and pH (Figure 4a), as discussed in the subsequent sections. Figure S4 and Text S4 in Supporting Information S1 shows the evolution of the gas content along the length of the porous medium after 8, 12, 14, and 25 hr. Additionally, MRI scans are compared to corresponding images from the pH indicator test (Figures 2b and 4, see Text S2 in Supporting Information S1 for details on pH determination and Movie S2 available online for complete time lapse of injection with methylthymol blue). For the first 14 hr, the pH in the q2-layer remains stable, ranging between 6 and 7. Following this period, the pH declines sharply over the course of 5 hr, reaching a value of 1—matching the pH of the injected solution by the 20-hr mark. Thereafter, the pH remains constant at 1 until the end of experiment. The pH decrease approximately coincides with the abrupt rise of pCO_2 (Figure 4).

Furthermore, MRI findings are supported by the in situ measurements of the partial pressure of aqueous CO_2 (Figure 4a). Initially, pCO_2 remains low and stable at approximately 3.02 hPa for the first 9 hours, then rises sharply to a maximum of 111.99 hPa at 25 hr, after which it steadily declines. This decrease may be due to continuous solution injection, displacing aqueous CO_2 from the pore space in the q2-layer. Unlike pCO_2, the relative gas content (Figures 3a and 3b) does not show this decline, likely because it is averaged across the entire q2-layer, while pCO_2 is measured at a single point. Overall, the observations align with other experimental findings, which estimate the reaction duration as 25 hr.

A similar trend is also observed during the monitoring of the differential pressure over 48 hr, here shown as the change of relative differential pressure (Figure 4b). For the first 18.5 hr, the differential pressure fluctuates minimally, within 4. It then increases, peaking at 10.5 at 24 hr, before declining to 7. The outlier at 29.5 hr is due to a syringe refill (shown in red in Figure 4b). The delayed pressure increase, compared to the rise in pCO_2, likely

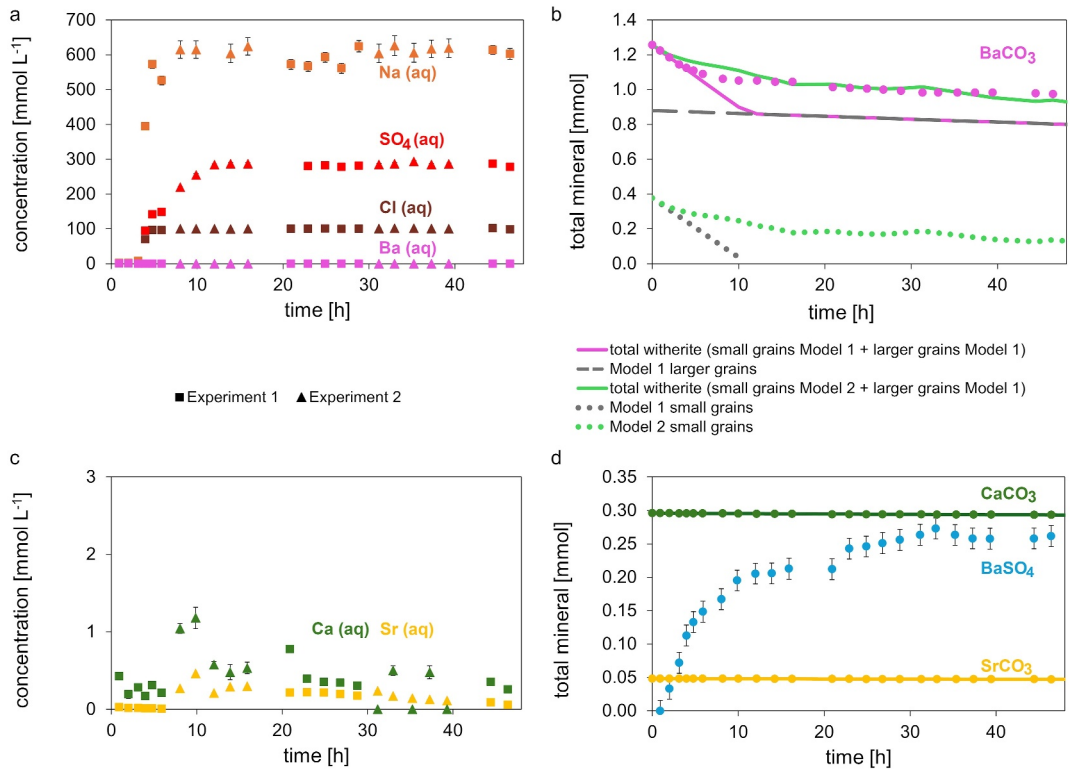

Figure 5. Aqueous anion and cation concentrations and total mineral evolution during the experiment. (a) Aqueous concentration of SO_4^{2-}, Ba^{2+}, Na^{+}, and Cl^{-}. Squares and triangles indicate samples from two experiments to test reproducibility. (b) Evolution of total mineral amount of $BaCO_3$ during the experiment. Gray dotted line represents modeled dissolution of small mineral grains and dashed gray line larger witherite grains after Model 1, also used for Model 2, Equation 4. Solid pink line shows total modeled dissolution with reactive surface area Model 1. Light green dotted line shows the modeled dissolution of small mineral grains after Model 2, Equation 6. Solid light green line represents the total modeled dissolution after Model 2. (c) Aqueous concentration of Sr^{2+} and Ca^{2+}. Squares and triangles indicate samples from different experiments to test reproducibility. (d) Evolution of total mineral amount of $CaCO_3$, $SrCO_3$, and $BaSO_4$ during the experiment. Solid lines represent dissolution of $CaCO_3$ and $SrCO_3$ following Model 1.

results from the time required for sufficient barite precipitation in the pore space to generate a measurable differential pressure change and therefore a change in permeability.

3.2. Mineral Transformation

The ion concentrations in the collected effluent as a function of time are shown in Figures 5a and 5c; measured values are presented in Table S3 and Text S3 in Supporting Information S1. Using the chemical composition of the sampled effluent, initial $BaCO_3$ amount, and known Na_2SO_4 input, the dissolution rate of $BaCO_3$ and precipitated $BaSO_4$ amount were calculated considering mass balance.

Two experiments were combined to achieve a regular sampling of the effluent during 48 hr. During the experiments, aqueous chloride ($Cl_{(aq)}$, Figure 5a) is detected after 3.1 hr, matching the time to fill the dead volume of the outlet tubing and the theoretically calculated residence time of the injected solution in the system. Over time, the Cl-concentration increases to match the injected value (100 mmol L^{-1}) and remains constant thereafter. The aqueous Na ($Na_{(aq)}$, Figure 5a) concentration behaves similarly. After 4.8 hr, the measured concentration matches the inlet concentration of 600 mmol L^{-1} and stays constant with time. It also fits the theoretically calculated residence time (4.2 hr) of the injected solution. Both ions do not participate in the chemical reaction, thus showing the breakthrough of the injected solution at the outlet. The aqueous concentration of Ba (Figure 5a) in the effluent is zero for the majority of sampled solutions, with the exception of the first two samples. Since Ba was not detected in the effluent beyond the initial samples, it is assumed that the Ba released from the dissolution of $BaCO_3$ is entirely consumed by the precipitation of $BaSO_4$. The aqueous sulfate (Figure 5a) measured in the

effluent approaches the inlet concentration after roughly 10 hr, however it never reaches the inlet concentration of 300 mmol L^{-1}. The mean value of the aqueous sulfate concentration after 10 hr until the end of the experiment is 285.04 mmol L^{-1}. This suggests that the precipitation of $BaSO_4$ significantly slows down after 10 hr, implying that the dissolution of $BaCO_3$ is inhibited, but never fully stops. The precipitation of barite is limited by the availability of Ba, which is supplied through the dissolution of $BaCO_3$. Notably, the concentration of aqueous strontium (Figure 5c) in the effluent remains non-zero throughout the reaction, although, it decreases with time. A similar trend is observed for aqueous Ca in the effluent (Figure 5c), indicating the continuous dissolution of $CaCO_3$. The variation in measured concentration of Sr and Ca can be explained by the inherent mineralogical heterogeneity of the natural witherite source material used in the experiment. The mineral amount of $BaCO_3$, $BaSO_4$, $CaCO_3$, and $SrCO_3$, as presented in Tabel S3, are obtained through mass balance calculations considering originally used molar amount of mineral, molar amount of injected solution, and molar amount of dissolved mineral in the collected effluent. Precipitation of $BaSO_4$ is estimated from the consumption of sulfate. In our experiment, 0.29 mmol of $BaCO_3$ dissolved and consequently 0.29 mmol of $BaSO_4$ precipitated from dissolved Ba and injected $SO^{2-}_{4(aq)}$. The amount of precipitate accounts for a calculated porosity decrease of 7% from 0.29 to 0.27, based on the difference of molar volumes of $BaCO_3$ and $BaSO_4$. The total amount of $BaCO_3$ over time is presented in Figure 5b and of $BaSO_4$ in Figure 5d, respectively (see Table S3 for data). During the initial 10 hours of reaction, the dissolution of $BaCO_3$ (Figure 5b) progresses at an accelerated rate of -9.5×10^{-9} mol s^{-1}, accounting for the majority of dissolution with 0.21 mmol of dissolved mineral. Subsequently, the dissolution of $BaCO_3$ decreases to -2.6×10^{-10} mol s^{-1}, representing a slow but continuous dissolution until the end of the experiment. During this time 0.08 mmol of $BaCO_3$ dissolved. The precipitation rates and the amount of $BaSO_4$ (Figure 5d) behaves directly inverse to the $BaCO_3$ dissolution. The total amount of $CaCO_3$ and $SrCO_3$ over time is presented in Figure 5d. The measured effluent concentration revealed that 0.003 mmol of $CaCO_3$ and 0.001 mmol of $SrCO_3$ dissolved over time. Both mineral phases show a constant dissolution with dissolution rates of -1.5×10^{-11} and -6.5×10^{-12} mol s^{-1}, respectively.

3.3. Micro-Structural Analysis of the Reacted $BaCO_3$

The reacted porous media was characterized with a combination of SEM (Figures 6a–6c, 6f, and 7b), EDS mapping (Figures 6d and 6e), and 3D Raman mapping (Figure 7a). Backscattered-electron (BSE) images (Figures 6a–6c and 6f) are based on the *Z*-contrast, so the difference of the atomic number *Z* of the used elements. Heavier phases appear light, lighter phases appear dark. In Figures 6a–6c and 6f pores appear black, $BaCO_3$ appears white and $BaSO_4$ appears in gray levels.

These analyses indicate that the whole pore space in the $BaCO_3$ layer is filled with $BaSO_4$ precipitate (Figures 6a and 6b). A few SiO_2 grains were cemented at the boundary of the q1 and q2-layer toward the w-layer. Larger witherite grains are surrounded by a shell of barite precipitate, while smaller witherite crystals have dissolved almost completely. Some smaller undissolved crystals are present in regions of localized clogging. $BaSO_4$ mainly occurs as round structures, suggesting heterogeneous nucleation of barite on the surface of CO_2 gas bubbles generated during witherite dissolution. 3D Raman mapping confirms that these structures are three dimensional further supporting the hypothesis that the precipitation occurs on the gas bubbles (Figures 6a–6c and 7a). The larger the pore space, the larger the gas bubbles can grow. The rim of the precipitate surrounding the gas bubbles is typically a few nm to μm thick and can also show spherical layering (Figure 6b). Homogeneous nucleation of barite leading to a possibly nano-crystalline precipitate in the pore space cannot be excluded (Figures 6a–6c). The findings of a similar nano-crystalline phase are reported in the literature when using a highly concentrated $BaCl_2$ solution for barite precipitation (Poonoosamy et al., 2016). The precipitate forms a shell around the $BaCO_3$ mineral grains. A gap between the precipitate and the reactive material can be observed (Figures 6b and 6c) suggesting coupled dissolution and precipitation processes rather than pseudomorphic replacement reactions (e.g., Forjanes et al., 2020; Kim et al., 2021; A. Putnis, 2009; Rendón-Angeles et al., 2008). In regions with fewer gas bubbles, no gap is present between the primary and secondary mineral phase (Figure 6e), suggesting a possible epitaxial growth of $BaSO_4$ on $BaCO_3$, given their shared orthorhombic crystal structure. On the surface of the reacted material barite crystals precipitated as platelets with a size of ca. 2–5 μm, mostly hexagonal in shape, often exhibiting twinning (Figure 7b).

$SrCO_3$ grains exhibit dissolution channels up to 50 μm deep, no passivation of the mineral surface, and only a minimal amount of precipitate observed close to the grain (Figure 6f). This supports the findings of Section 3.2

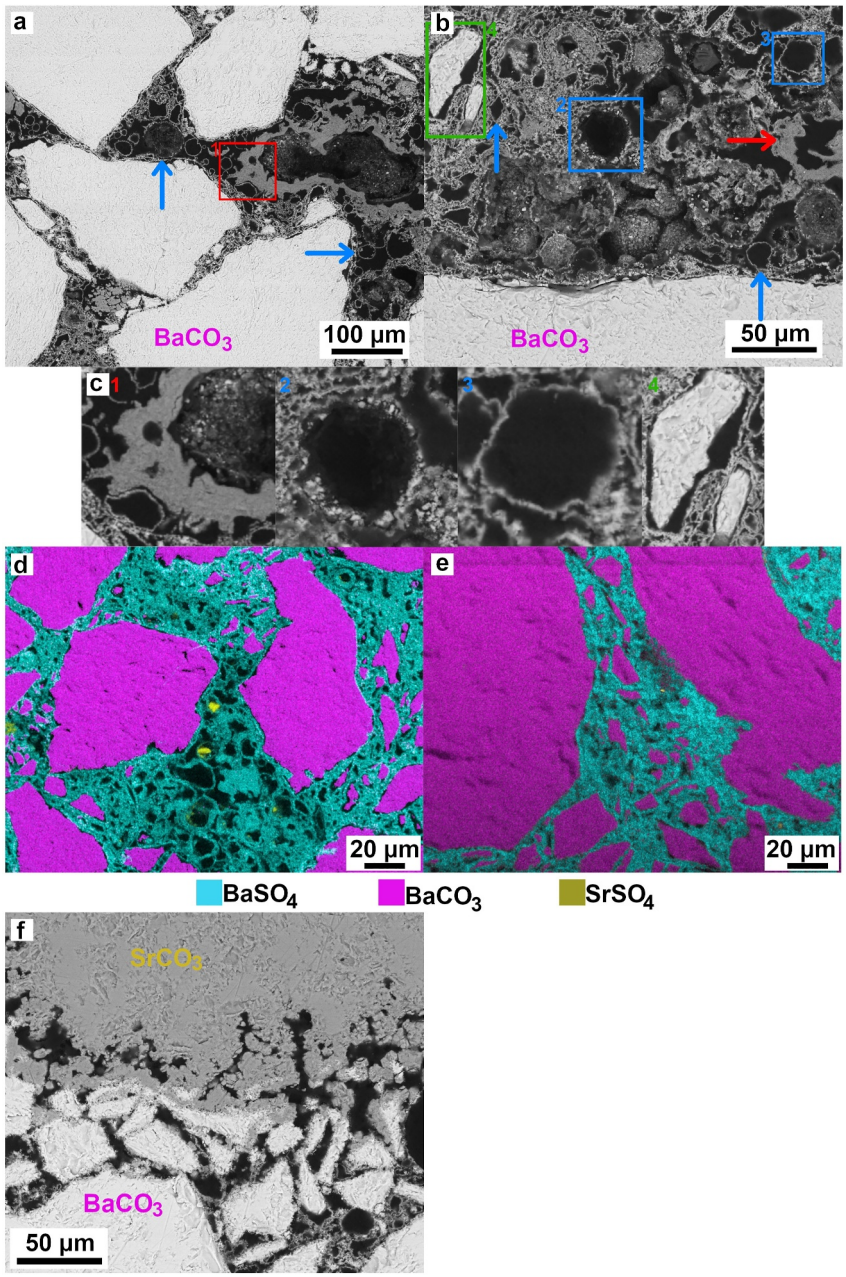

Figure 6. Micro-structural analysis of the reacted witherite layer impregnated with resin. (a) scanning electron microscopy (SEM) image overview of pore space with precipitate on gas bubbles (blue arrow) and possible nano-crystalline phase (red square). (b) SEM image of reacted witherite layer with gas bubbles (blue arrow) covered with precipitate and mineral armoring around witherite grains (green square). Possible nano-crystalline phase (red arrow). (c) Detailed images. (1) Possible nano-crystalline phase, (2) and (3) gas bubble covered with precipitate, and (4) mineral armoring around witherite grains. (d) energy dispersive X-ray spectroscopy (EDS) map of reacted w-layer. Overview of the pore space with precipitate. Determination of $BaCO_3$ is based on Ba-K measurement, of $BaSO_4$ on S-K measurement, and of $SrSO_4$ on Sr-L measurement. Possibly nano-crystalline precipitate present. (e) EDS map of a location with no gas bubbles. (f) SEM image of sample with dissolution pathways in $SrCO_3$ grain in comparison to $BaCO_3$ grain.

that $SrCO_3$ is being dissolved throughout the entire experiment. The decrease in aqueous Sr concentration over time is likely attributed to the reduced accessibility of the pore space, resulting from the accumulation of trapped gas bubbles and the precipitation of $BaSO_4$, which in turn decreases the reactive surface areas. Elemental mapping reveals isolated regions where $SrSO_4$ appears to have precipitated (Figures 6d and 6e). However, it is essential to note that the Si(K) line overlaps with the Sr(L) line in the EDS spectrum, which may lead to artefacutal signals.

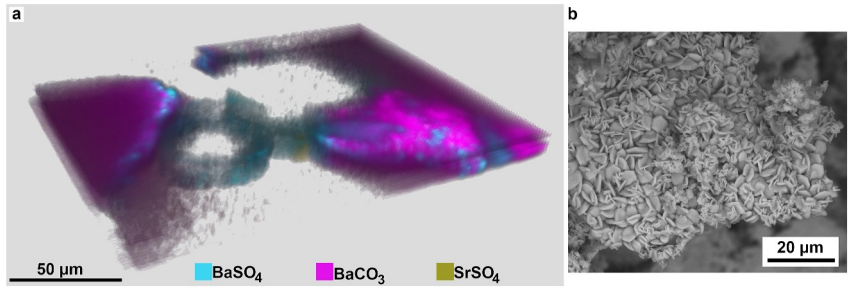

Figure 7. Micro-structural analysis of the reacted and dried witherite layer. (a) 3D Raman map of reacted and dried sample. (b) scanning electron microscopy image of barite precipitates on the surface of the reacted sample.

Furthermore, the polishing process may have introduced contamination with quartz sand from the q1 and q2-layer, potentially contributing to the observed Sr signal.

4. Discussion

In this section, we evaluate and discuss classically employed theoretical models that describe the mineralogical reactivity and transport properties of the system and address the challenges of describing CDPG using reactive transport models.

4.1. Mineral Reactivity

Our results show that MRI real-time monitoring can effectively capture the complex coupled process of witherite dissolution and barite precipitation, involving simultaneous production of gaseous CO_2 induced through the injection of an acidic solution in the system. The release of CO_2 is also accompanied by the release of $Ba_{(aq)}$. The continuously injected sulfate ions in the pore water react with the released Ba^{2+} to precipitate as barite on the surface of the gas bubbles which act as active sites for the nucleation of barite. The electric charge and the zeta potential at the surface of the CO_2 bubble may play a role on the distribution of solutes (attraction SO_4^{2-} species) depending on the local value of the pH (Leroy et al., 2012), which may favor the precipitation of barite.

We evaluated the mineral dissolution with two commonly employed reactive surface area models to describe the observed dissolution patterns (Figures 5b and 5d). Dissolution rate of the witherite crystals, dm/dt (mol s^{-1}), are based on the equation given by Palandri and Kharaka (2004):

$$dm/dt = -S_A k_r (a_{H^+})(1 - \Omega) \tag{4}$$

where S_A (m^2) is the reactive surface area, k_r (mol m^{-2} s^{-1}) is the acidic dissolution rate constant at 298.15 K, a_{H^+} is the activity of H^+, and Ω is the saturation state of the solution. Dissolution rate constants are reported in Table 2. No literature values for the acidic dissolution of strontianite are currently available. However, its dissolution behavior is expected to be proportional to the dissolution of calcite, so the dissolution rate constant for calcite was used for strontianite here (Oelkers & Addassi, 2025).

Two reactive surface area models were tested to fit the experimental dissolution rates calculated from effluent concentrations (Figures 5b and 5d, and Table S3). In Model 1, the reactive surface area, S_A (m^2), scales linearly to the volume of the mineral:

$$S_A = V_i a_i \tag{5}$$

where S_A (m^2) is the reactive surface area, V_i (m^3) is the volume of the mineral, and a_i (m^2 m^{-3}) is the mineral's specific surface area (i.e., surface area per unit volume of the mineral phase). In the model, the dissolution of witherite (Figure 5b), strontianite, and calcite (Figure 5d) were considered separately.

Model 2 considers a reduced mineral reactivity due to surface passivation by the precipitation of secondary minerals following Daval et al. (2009) and Poonoosamy, Klinkenberg, et al. (2020):

$$S_{A(t)} = a[V_{wit(0)} - K_p(V_{precipitate(t)})^p] \tag{6}$$

where a (m^2 $m^{-3}_{mineral}$) is the specific surface area of the witherite grains, $V_{wit(0)}$ (m^3) is the initial volume of witherite, K_p a proportionality factor, here 1, $V_{precipitate}$ (m^3) is the volume of precipitated barite, and p is a fitting parameter related to the particle size distribution, here 1. For details refer to Text S3 in Supporting Information S1. In both of our models the specific surface area was fitted to match experimental results, as geometrical and BET surface areas often overestimate the reactive surface area since they do not consider the hydrological accessibility of the reactive phases (Helgeson et al., 1984; Maher et al., 2006; Molins et al., 2012; Peters, 2009).

The witherite dissolution modeled using Model 1 (Equation 4), is characterized by two distinct phases (Figure 5b, gray lines). Initially, the dissolution process is predominantly governed by the smaller grain fraction (Figure 5b, gray dotted line), followed by a transition to dominance by the larger grain fraction (Figure 5b, gray dashed lines). The specific surface area a_i of the small grains is fitted to 7.2×10^8 m^2 m^{-3}, whereas the specific surface area of the larger grains is fitted to 1.5×10^7 m^2 m^{-3}. Gray lines in Figure 5b show the two modeled trends individually and the solid pink line represents the combination of both trends. It becomes evident that Model 1 only captures the mineral transformation during the first hours of the experiment accurately, overestimating the dissolution dominated by the smaller grains at the later stages of the experiment.

Model 2 (Figure 5b, green lines) accounts for a passivation mechanism considering the volume of the precipitated secondary mineral phase. With respect to the findings from Model 1, we only applied Model 2 to the small grain fraction, as the dissolution during the first 10 hours is clearly dominated by this process. According to Model 2, 0.24 mmol (64%) of the small grain mineral fraction (Figure 5b, green dotted line) and only 0.08 mmol (10%) of the larger grain fraction (Figure 5b, gray dashed line) dissolved. The larger grain fraction is less reactive due to the smaller specific surface area and seems to undergo dissolution with a barite crust forming around it, passivating it and consequently further reducing its reactivity. The solid green line represents the total mineral content according to Model 2, which provides a more accurate representation of the dissolution process compared to Model 1 (solid pink line).

The dissolution of strontianite and calcite follow results of Model 1 closely, and are captured by the linear Model 1 accurately (Figure 5d). Although the presented models can be employed in a reactive transport model to describe the reaction, none of them explicitly account for a reduction of reactive surface area due to bubble formation as was observed in Soulaine et al. (2018). Future studies will include microfluidic experiments (Poonoosamy et al., 2019, 2023, 2024; Poonoosamy, Mahrous, et al., 2021) to systematically evaluate reactive surface areas, aiming to develop a comprehensive reactive surface area model for CDPG.

4.2. Porosity-Permeability-Relationship

The formation of barite in the presented case significantly changes the pore connectivity and most likely the absolute permeability which is reflected by the increase in the differential pressure measurement. The gas produced is transported through the witherite layer and the sand region but can also become trapped by the precipitating phase, further contributing to porosity clogging. The differential pressure measurement recorded during the reaction suggests that the permeability of the system is decreasing (see Text S2 in Supporting Information S1). Considering that the precipitate and the gas bubbles are clogging the pore space widely, this is an expected behavior. The effective permeability of the total system including all three layers is estimated to have decreased by one order of magnitude (Table 1).

The collected pressure data and the obtained relative gas content is used to determine the changes of the effective permeability in the q1 and q2-layer with time with a function after Van Genuchten (1980) and Mualem (1976) following the given equation:

$$K(S_e) = K_{sat} S_e^{\frac{1}{2}} \left(1 - \left(1 - S_e^{\frac{1}{m}}\right)^m\right)^2 \tag{7}$$

where K_{sat} (m s^{-1}) is the hydraulic conductivity of the fully saturated system, S_e is the effective saturation, and m is a fitting parameter, here fitted to $m = 4.8$, so that the effective permeability of the saturated system has the

same order of magnitude as the determined absolute permeability (see Text S2 in Supporting Information S1 for details). The effective permeability in q1 and q2 is estimated to decrease by one order of magnitude from 2.89×10^{-12} m^2 (determined with falling head method after Kresic (2006)) to 6.80×10^{-13} m^2 and 4.90×10^{-13} m^2 (see Table 1, Figure 4c), respectively. According to the Van Genuchten-Mualem equation the effective permeability in the q2-layer (Figure 4c) has an initial value of 1.06×10^{-12} m^2, steadily decreasing for 18.5 hr, then increasing suddenly and reaching a maximum after 20 hr, and finally decreasing again until it reaches the final value of 4.90×10^{-13} m^2. While the Van Genuchten-Mualem equation, along with the associated fitting parameters is, e.g., well-established for quartz sand, as used in the q1 and q2-layer (e.g., Léger et al., 2015; Luo et al., 2019; Mayenna & Khaleel, 2022), it cannot be directly applied to chemically evolving materials such as the w-layer. In this case, chemical reactions, including the precipitation of $BaSO_4$ and subsequent clogging of the pore space, significantly alter the geometry of the pore network, which is expected to have a substantial impact on the absolute permeability. Developing an appropriate equation to describe these processes remains a challenge. Commonly used models for characterizing relative permeability and capillary pressure-saturation relationships, such as the Brooks-Corey model (Brooks & Corey, 1966), do not account for the effects of chemical reactions. Future work will include tailored experiments, including time resolved X-ray computed tomography measurements as were done in Boon and Hajibeygi (2022), Jangda et al. (2023, 2024) for capillary pressure-saturation measurements in porous media that have undergone structure alteration due to mineral precipitation on gas bubbles. Results could help to derive new capillary pressure-saturation relationships, consequently overcoming the current limitations of this study.

4.3. Implications on Reactive Transport Models

Continuum-scale RTM can address the complex interactions between multi-phase fluid flows and mineralogical reactions (Seigneur et al., 2022; Sin et al., 2017, 2023; Soulaine, 2024). The empirical formulations used to describe these coupled hydrogeochemical processes are often simplified (Seigneur et al., 2019). For variably saturated porous media, the concept of relative permeability of the rock matrix is usually described in RTM by empirical functions, such as the Brooks and Corey equation or the Van Genuchten-Mualem equation, yet changes in transport properties of porous media depend on much more than changes in saturation (Adebimpe et al., 2024; Churakov & Prasianakis, 2018; Ladd & Szymczak, 2021; Maes & Menke, 2024; Mukherjee et al., 2023; Noiriel & Soulaine, 2021); they also depend on how reactions alter pore structure, pore connectivity, surface roughness, surface reactivity and wettability of minerals.

Simulating dynamic, multi-phase processes, as presented in this study, poses great challenges for commonly used RTM codes, such as TOUGHREACT (T. Xu et al., 2011) and PFLOTRAN (Hammond et al., 2014), which are widely adopted for simulating multi-phase fluid flow. Reactive transport modeling codes can simulate mineral dissolution and gas production and migration separately. Soulaine et al. (2018) developed a micro-continuum Darcy-Brinkman-Stokes model (Soulaine et al., 2017) that successfully integrated the dissolution of a carved calcite array with the generation of CO_2 gas bubbles, implementing it within the finite-volume OpenFOAM simulation framework. Similarly, Vehling and Shao (2023) expanded on a numerical model for reactive multi-component two-phase transport in the OpenGeoSys (Lu et al., 2022) framework (Huang et al., 2021), focusing on gas production and the dissolution of concrete aggregates in the context of deep geological nuclear waste disposal. Neither of these studies consider coupled precipitation processes, as examined in the current work, so their findings do not fully contribute to a realistic RTM code that accounts for all processes. Currently, to our knowledge, no existing code simultaneously couples all these processes. This is primarily due to the widely implemented global implicit, sequential iteration, and sequential non-iteration approaches, which only couple solute transport and chemical reaction equations but not fluid flow equations (Seigneur et al., 2023). Although these approaches are numerically efficient and act well in approximating single-phase reactive fluid flow, they are insufficient to account for more complex systems in which chemical reactions significantly affect fluid flow, particularly in cases involving gas generation, exsolution and subsequent migration in multi-phase RTM systems, as observed in this study. Therefore, more sophisticated mathematical coupling approaches are needed to enable realistic simulations of such processes. The interplay between coupled mineral dissolution/precipitation and gas generation involves complex phenomena such as mineral passivation, permanent pore clogging due to mineral precipitation, and transient pore clogging from gas generation. Accurately capturing these processes requires much more advanced, realistic porosity-permeability relationships and relative permeability models that are not yet available in current literature. Further research is warranted to develop and implement these refined models

within reactive transport codes, enabling the simulation of such processes in both experimental and applied conditions.

5. Conclusion

We developed a novel 3D reactive transport experiment to investigate the coupled processes of witherite dissolution, barite precipitation, and CO_2 exsolution. The transition from fully saturated to partially saturated conditions was monitored using time-resolved Nuclear MRI, which revealed the heterogeneous formation of gas enriched regions downstream in the quartz layer while the gas content in the reacting layer remained fairly uniform. Gas production was successfully monitored in real-time, becoming detectable after 8 hr and continuing until 25 hr in total, with gas saturation stabilizing at approximately 10% in localized regions. Effluent ion concentration measurements allowed for the assessment of bulk mineral evolution. Reactive surface area modeling indicated that dissolution was initially accelerated by the higher reactivity of smaller witherite grains, reflected as 64% of the small witherite fraction dissolved during the reaction and only 10% of the larger mineral grain fraction, but subsequently slowed down due to surface passivation caused by mineral armoring, aligning more closely with observed dissolution trends. The reduction in porosity of the reactive porous media was determined from mineral mass balance calculations, showing a 7% decrease in porosity, accompanied by an 11% increase in differential pressure. Micro-structural analysis supported porosity and permeability decrease as it revealed that barite precipitates on the surface of witherite grains, gas bubbles, and within pore spaces, leading to localized porosity clogging and reducing hydrological accessibility to the unreacted witherite for further dissolution. Simulating these dynamic, multi-phase processes pose challenges for current reactive transport models which lack comprehensive coupling of solute transport, fluid flow, and gas generation. Small-scale experiments like ours highlight complexities such as gas exsolution contribution to pore clogging and mineral passivation that require more advanced modeling approaches. Our findings provide valuable data to benchmark and refine RTMs, for realistic process description.

Data Availability Statement

The data used for the presented experiments in the study are available at Jülich DATA via https://doi.org/10.26165/JUELICH-DATA/OBASAC (Wegner et al., 2024) with Creative Commons CC-BY 4.0—"Attribution" with no further registration required.

Acknowledgments
The main research leading to these results has received funding from the European Research Council through the project GENIES (ERC grant agreement 101040341). The authors would like to acknowledge Daniel Hintzen for the fabrication of the Plexiglas reactor, Murat Güngör for support of SEM and EDS investigations, Philip Kegler for support of XRD investigations, Alexander Kaspor for support of Raman investigations, Guido Deissmann for considerably improving the manuscript, and Cyprien Soulaine for fruitful discussions. Furthermore, the first author would like to thank the Mineralogical Museum of the University Bonn and A. Weiß for providing the witherite sample. Open Access funding enabled and organized by Projekt DEAL.

References

Adebimpe, A. I., Foroughi, S., Bijeljic, B., & Blunt, M. J. (2024). Percolation without trapping: How Ostwald ripening during two-phase displacement in porous media alters capillary pressure and relative permeability. *Physical Review E*, *110*(3), 035105. https://doi.org/10.1103/PhysRevE.110.035105

Ahmadi, N., Acocella, M., Fries, E., Mosthaf, K., & Rolle, M. (2022). Oxygen propagation fronts in porous media under evaporative conditions at the soil/atmosphere interface: Lab-scale experiments and model-based interpretation. *Water Resources Research*, *58*(6), e2021WR031668. https://doi.org/10.1029/2021WR031668

Beckingham, L. E. (2017). Evaluation of macroscopic porosity-permeability relationships in heterogeneous mineral dissolution and precipitation scenarios. *Water Resources Research*, *53*(12), 10217–10230. https://doi.org/10.1002/2017WR021306

Boampong, L. O., Hyman, J. D., Carey, W. J., Viswanathan, H. S., & Navarre-Sitchler, A. (2024). Characterizing the combined impact of nucleation-driven precipitation and secondary passivation on carbon mineralization. *Chemical Geology*, *663*, 122256. https://doi.org/10.1016/j.chemgeo.2024.122256

Boon, M., & Hajibeygi, H. (2022). Experimental characterization of H_2/water multiphase flow in heterogeneous sandstone rock at the core scale relevant for underground hydrogen storage (UHS). *Scientific Reports*, *12*(1), 14604. https://doi.org/10.1038/s41598-022-18759-8

Brooks, R. H., & Corey, A. T. (1966). Properties of porous media affecting fluid flow. *Journal of the Irrigation and Drainage Division*, *92*(2), 61–88. https://doi.org/10.1061/JRCEA4.0000425

Chagneau, A. (2015). *The effects of porosity clogging on the transport properties of porous materials under geochemical perturbation: Experimental approach and modeling*. Freie Universität Berlin. https://doi.org/10.17169/refubium-9656

Chagneau, A., Claret, F., Enzmann, F., Kersten, M., Heck, S., Madé, B., & Schäfer, T. (2015). Mineral precipitation-induced porosity reduction and its effect on transport parameters in diffusion-controlled porous media. *Geochemical Transactions*, *16*, 1–16. https://doi.org/10.1186/s12932-015-0027-z

Chou, L., Garrels, R. M., & Wollast, R. (1989). Comparative study of the kinetics and mechanisms of dissolution of carbonate minerals. *Chemical Geology*, *78*(3–4), 269–282. https://doi.org/10.1016/0009-2541(89)90063-6

Churakov, S. V., & Prasianakis, N. I. (2018). Review of the current status and challenges for a holistic process-based description of mass transport and mineral reactivity in porous media. *American Journal of Science*, *318*(9), 921–948. https://doi.org/10.2475/09.2018.03

Daval, D., Martinez, I., Corvisier, J., Findling, N., Goffé, B., & Guyot, F. (2009). Carbonation of ca-bearing silicates, the case of wollastonite: Experimental investigations and kinetic modeling. *Chemical Geology*, *265*(1–2), 63–78. https://doi.org/10.1016/j.chemgeo.2009.01.022

Deng, H., Gharasoo, M., Zhang, L., Dai, Z., Hajizadeh, A., Peters, C. A., et al. (2022). A perspective on applied geochemistry in porous media: Reactive transport modeling of geochemical dynamics and the interplay with flow phenomena and physical alteration. *Applied Geochemistry*, *146*, 105445. https://doi.org/10.1016/j.apgeochem.2022.105445

El Mendili, Y., Abdelouas, A., Karakurt, G., Chaou, A. A., Essehli, R., Bardeau, J.-F., & Grenèche, J.-M. (2015). The effect of temperature on carbon steel corrosion under geological conditions. *Applied Geochemistry*, *52*, 76–85. https://doi.org/10.1016/j.apgeochem.2014.11.008

Emmanuel, S., & Berkowitz, B. (2005). Mixing–induced precipitation and porosity evolution in porous media. *Advances in Water Resources*, *28*(4), 337–344. https://doi.org/10.1016/j.advwatres.2004.11.010

Fabich, H. T., Sederman, A. J., & Holland, D. J. (2016). Development of ultrafast UTE imaging for granular systems. *Journal of Magnetic Resonance*, *273*, 113–123. https://doi.org/10.1016/j.jmr.2016.10.016

Forjanes, P., Astilleros, J. M., & Fernández-Díaz, L. (2020). The formation of barite and celestite through the replacement of gypsum. *Minerals*, *10*(2), 189. https://doi.org/10.3390/min10020189

Haberer, C. M., Muniruzzaman, M., Grathwohl, P., & Rolle, M. (2015). Diffusive–dispersive and reactive fronts in porous media: Iron(II) oxidation at the unsaturated–saturated interface. *Vadose Zone Journal*, *14*(5), 1–14. https://doi.org/10.2136/vzj2014.07.0091

Hammond, G. E., Lichtner, P. C., & Mills, R. (2014). Evaluating the performance of parallel subsurface simulators: An illustrative example with PFLOTRAN. *Water Resources Research*, *50*(1), 208–228. https://doi.org/10.1002/2012WR013483

Helgeson, H. C., Murphy, W. M., & Aagaard, P. (1984). Thermodynamic and kinetic constraints on reaction rates among minerals and aqueous solutions. II. Rate constants, effective surface area, and the hydrolysis of feldspar. *Geochimica et Cosmochimica Acta*, *48*(12), 2405–2432. https://doi.org/10.1016/0016-7037(84)90294-1

Huang, Y., Shao, H., Wieland, E., Kolditz, O., & Kosakowski, G. (2021). Two-phase transport in a cemented waste package considering spatio-temporal evolution of chemical conditions. *npj Materials Degradation*, *5*(1), 4. https://doi.org/10.1038/s41529-021-00150-z

Hummel, W., & Thoenen, T. (2021). *The PSI chemical thermodynamic data base 2020. Nagra Technical Report NTB 21-03*. Nagra.

Jangda, Z., Menke, H., Busch, A., Geiger, S., Bultreys, T., Lewis, H., & Singh, K. (2023). Pore-scale visualization of hydrogen storage in a sandstone at subsurface pressure and temperature conditions: Trapping, dissolution and wettability. *Journal of Colloid and Interface Science*, *629*, 316–325. https://doi.org/10.1016/j.jcis.2022.09.082

Jangda, Z., Menke, H., Busch, A., Geiger, S., Bultreys, T., & Singh, K. (2024). Subsurface hydrogen storage controlled by small-scale rock heterogeneities. *International Journal of Hydrogen Energy*, *60*, 1192–1202. https://doi.org/10.1016/j.ijhydene.2024.02.233

Jenni, A., Gimmi, T., & Mäder, U. (2024). Coupling of porosity and diffusive transport in highly reactive systems: Open issues of reactive transport modelling. *Applied Geochemistry*, *170*, 106076. https://doi.org/10.1016/j.apgeochem.2024.106076

Jiang, F., & Tsuji, T. (2014). Changes in pore geometry and relative permeability caused by carbonate precipitation in porous media. *Physical Review E*, *90*(5), 053306. https://doi.org/10.1103/PhysRevE.90.053306

Kang, Q., Zhang, D., & Chen, S. (2003). Simulation of dissolution and precipitation in porous media. *Journal of Geophysical Research*, *108*(B10), 154701. https://doi.org/10.1029/2003JB002504

Katz, G. E., Berkowitz, B., Guadagnini, A., & Saaltink, M. W. (2011). Experimental and modeling investigation of multicomponent reactive transport in porous media. *Journal of Contaminant Hydrology*, *120*, 27–44. https://doi.org/10.1016/j.jconhyd.2009.11.002

Kim, Y., Abdilla, B., Yuan, K., De Andrade, V., Sturchio, N. C., Lee, S. S., & Fenter, P. (2021). Replacement of calcium carbonate polymorphs by cerussite. *ACS Earth and Space Chemistry*, *5*(9), 2433–2441. https://doi.org/10.1021/acsearthspacechem.1c00177

Kresic, N. (2006). *Hydrogeology and groundwater modeling*. CRC Press. https://doi.org/10.1201/9781420004991

Krevor, S. C., Pini, R., Li, B., & Benson, S. M. (2011). Capillary heterogeneity trapping of CO_2 in a sandstone rock at reservoir conditions. *Geophysical Research Letters*, *38*(15), L15401. https://doi.org/10.1029/2011gl048239

Ladd, A. J., & Szymczak, P. (2021). Reactive flows in porous media: Challenges in theoretical and numerical methods. *Annual Review of Chemical and Biomolecular Engineering*, *12*(1), 543–571. https://doi.org/10.1146/annurev-chembioeng-092920-102703

Lefeuvre, N., Truche, L., Donzé, F.-V., Gal, F., Tremosa, J., Fakoury, R.-A., et al. (2022). Natural hydrogen migration along thrust faults in foothill basins: The North Pyrenean Frontal Thrust case study. *Applied Geochemistry*, *145*, 105396. https://doi.org/10.1016/j.apgeochem.2022.105396

Léger, E., Saintenoy, A., Tucholka, P., & Coquet, Y. (2015). Inverting surface gpr data to estimate wetting and drainage water retention curves in laboratory. In *2015 8th international workshop on advanced ground penetrating radar (iwagpr)* (pp. 1–5). https://doi.org/10.1109/IWAGPR.2015.7292672

Leroy, P., Jougnot, D., Revil, A., Lassin, A., & Azaroual, M. (2012). A double layer model of the gas bubble/water interface. *Journal of Colloid and Interface Science*, *388*(1), 243–256. https://doi.org/10.1016/j.jcis.2012.07.029

Li, Q., Steefel, C. I., & Jun, Y.-S. (2017). Incorporating nanoscale effects into a continuum-scale reactive transport model for CO_2-deteriorated cement. *Environmental Science & Technology*, *51*(18), 10861–10871. https://doi.org/10.1021/acs.est.7b00594

Lönartz, M. I., Yang, Y., Deissmann, G., Bosbach, D., & Poonoosamy, J. (2023). Capturing the dynamic processes of porosity clogging. *Water Resources Research*, *59*(11), e2023WR034722. https://doi.org/10.1029/2023WR034722

Lu, R., Nagel, T., Poonoosamy, J., Naumov, D., Fischer, T., Montoya, V., et al. (2022). A new operator-splitting finite element scheme for reactive transport modeling in saturated porous media. *Computers & Geosciences*, *163*, 105106. https://doi.org/10.1016/j.cageo.2022.105106

Luo, Z., Kong, J., Shen, C., Lu, C., Hua, G., Zhao, Z., et al. (2019). Evaluation and application of the modified Van Genuchten function for unsaturated porous media. *Journal of Hydrology*, *571*, 279–287. https://doi.org/10.1016/j.jhydrol.2019.01.051

Maes, J., & Menke, H. P. (2024). Dispersivity calculation in digital twins of multiscale porous materials using the micro-continuum approach. *Journal of Environmental Chemical Engineering*, *12*(5), 113729. https://doi.org/10.1016/j.jece.2024.113729

Maher, K., Steefel, C. I., DePaolo, D. J., & Viani, B. E. (2006). The mineral dissolution rate conundrum: Insights from reactive transport modeling of U isotopes and pore fluid chemistry in marine sediments. *Geochimica et Cosmochimica Acta*, *70*(2), 337–363. https://doi.org/10.1016/j.gca.2005.09.001

Mayenna, A., & Khaleel, R. (2022). Moisture-dependent anisotropy calculations using the Van Genuchten–Mualem model. *Vadose Zone Journal*, *21*(3), e20191. https://doi.org/10.1002/vzj2.20191

Molins, S., Trebotich, D., Steefel, C. I., & Shen, C. (2012). An investigation of the effect of pore scale flow on average geochemical reaction rates using direct numerical simulation. *Water Resources Research*, *48*(3), W03527. https://doi.org/10.1029/2011WR011404

Mualem, Y. (1976). A new model for predicting the hydraulic conductivity of unsaturated porous media. *Water Resources Research*, *12*(3), 513–522. https://doi.org/10.1029/WR012i003p00513

Mukherjee, S., Johns, R. T., Foroughi, S., & Blunt, M. J. (2023). Fluid-fluid interfacial area and its impact on relative permeability: A pore network modeling study. *SPE Journal*, *28*(2), 653–663. https://doi.org/10.2118/209445-PA

Muniruzzaman, M., Haberer, C. M., Grathwohl, P., & Rolle, M. (2014). Multicomponent ionic dispersion during transport of electrolytes in heterogeneous porous media: Experiments and model-based interpretation. *Geochimica et Cosmochimica Acta*, *141*, 656–669. https://doi.org/10.1016/j.gca.2014.06.020

Noiriel, C., & Soulaine, C. (2021). Pore-scale imaging and modelling of reactive flow in evolving porous media: Tracking the dynamics of the fluid–rock interface. *Transport in Porous Media*, *140*(1), 181–213. https://doi.org/10.1007/s11242-021-01613-2

Oelkers, E. H., & Addassi, M. (2025). A comprehensive and consistent mineral dissolution rate database: Part III: Non-silicate minerals including carbonate, sulfate, phosphate, halide, and oxy-hydroxide minerals. *Chemical Geology*, *673*, 122528. https://doi.org/10.1016/j.chemgeo.2024.122528

Osselin, F., Pichavant, M., Champallier, R., Ulrich, M., & Raimbourg, H. (2022). Reactive transport experiments of coupled carbonation and serpentinization in a natural serpentinite. implication for hydrogen production and carbon geological storage. *Geochimica et Cosmochimica Acta*, *318*, 165–189. https://doi.org/10.1016/j.gca.2021.11.039

Osselin, F., Soulaine, C., Fauguerolles, C., Gaucher, E., Scaillet, B., & Pichavant, M. (2022). Orange hydrogen is the new green. *Nature Geoscience*, *15*(10), 765–769. https://doi.org/10.1038/s41561-022-01043-9

Palandri, J. L., & Kharaka, Y. K. (2004). *A compilation of rate parameters of water-mineral interaction kinetics for application to geochemical modeling*. US Geological Survey. https://doi.org/10.3133/ofr20041068

Peters, C. A. (2009). Accessibilities of reactive minerals in consolidated sedimentary rock: An imaging study of three sandstones. *Chemical Geology*, *265*(1–2), 198–208. https://doi.org/10.1016/j.chemgeo.2008.11.014

Plummer, L., & Busenberg, E. (1987). Thermodynamics of aragonite-strontianite solid solutions: Results from stoichiometric solubility at 25 and 76°C. *Geochimica et Cosmochimica Acta*, *51*(6), 1393–1411. https://doi.org/10.1016/0016-7037(87)90324-3

Poonoosamy, J., Curti, E., Kosakowski, G., Grolimund, D., Van Loon, L., & Mäder, U. (2016). Barite precipitation following celestite dissolution in a porous medium: A SEM/BSE and μ-XRD/XRF study. *Geochimica et Cosmochimica Acta*, *182*, 131–144. https://doi.org/10.1016/j.gca.2016.03.011

Poonoosamy, J., Haber-Pohlmeier, S., Deng, H., Deissmann, G., Klinkenberg, M., Gizatullin, B., et al. (2020). Combination of MRI and SEM to assess changes in the chemical properties and permeability of porous media due to barite precipitation. *Minerals*, *10*(3), 226. https://doi.org/10.3390/min10030226

Poonoosamy, J., Kaspor, A., Schreinemachers, C., Bosbach, D., Cheong, O., Kowalski, P. M., & Obaied, A. (2024). A radiochemical lab-on-a-chip paired with computer vision to unlock the crystallization kinetics of $(Ba,Ra)SO_4$. *Scientific Reports*, *14*(1), 9502. https://doi.org/10.1038/s41598-024-59888-6

Poonoosamy, J., Klinkenberg, M., Deissmann, G., Brandt, F., Bosbach, D., Mäder, U., & Kosakowski, G. (2020). Effects of solution supersaturation on barite precipitation in porous media and consequences on permeability: Experiments and modelling. *Geochimica et Cosmochimica Acta*, *270*, 43–60. https://doi.org/10.1016/j.gca.2019.11.018

Poonoosamy, J., Kosakowski, G., Van Loon, L. R., & Mäder, U. (2015). Dissolution–precipitation processes in tank experiments for testing numerical models for reactive transport calculations: Experiments and modelling. *Journal of Contaminant Hydrology*, *177*, 1–17. https://doi.org/10.1016/j.jconhyd.2015.02.007

Poonoosamy, J., Lu, R., Lönartz, M. I., Deissmann, G., Bosbach, D., & Yang, Y. (2022). A lab on a chip experiment for upscaling diffusivity of evolving porous media. *Energies*, *15*(6), 2160. https://doi.org/10.3390/en15062160

Poonoosamy, J., Mahrous, M., Curti, E., Bosbach, D., Deissmann, G., Churakov, S. V., et al. (2021). A lab-on-a-chip approach integrating in-situ characterization and reactive transport modelling diagnostics to unravel $(Ba,Sr)SO_4$ oscillatory zoning. *Scientific Reports*, *11*(1), 23678. https://doi.org/10.1038/s41598-021-02840-9

Poonoosamy, J., Obaied, A., Deissmann, G., Prasianakis, N. I., Kindelmann, M., Wollenhaupt, B., et al. (2023). Microfluidic investigation of pore-size dependency of barite nucleation. *Communications Chemistry*, *6*(1), 250. https://doi.org/10.1038/s42004-023-01049-3

Poonoosamy, J., Wanner, C., Alt Epping, P., Águila, J., Samper, J., Montenegro, L., et al. (2021). Benchmarking of reactive transport codes for 2D simulations with mineral dissolution–precipitation reactions and feedback on transport parameters. *Computational Geosciences*, *25*(4), 1337–1358. https://doi.org/10.1007/s10596-018-9793-x

Poonoosamy, J., Westerwalbesloh, C., Deissmann, G., Mahrous, M., Curti, E., Churakov, S. V., et al. (2019). A microfluidic experiment and pore scale modelling diagnostics for assessing mineral precipitation and dissolution in confined spaces. *Chemical Geology*, *528*, 119264. https://doi.org/10.1016/j.chemgeo.2019.07.039

Prasianakis, N. I., Curti, E., Kosakowski, G., Poonoosamy, J., & Churakov, S. V. (2017). Deciphering pore-level precipitation mechanisms. *Scientific Reports*, *7*(1), 13765. https://doi.org/10.1038/s41598-017-14142-0

Putnis, A. (2009). Mineral replacement reactions. *Reviews in Mineralogy and Geochemistry*, *70*(1), 87–124. https://doi.org/10.2138/rmg.2009.70.3

Putnis, C. V., & Putnis, A. (2022). A mechanism of ion exchange by interface-coupled dissolution-precipitation in the presence of an aqueous fluid. *Journal of Crystal Growth*, *600*, 126840. https://doi.org/10.1016/j.jcrysgro.2022.126840

Rajyaguru, A., L'Hôpital, E., Savoye, S., Wittebroodt, C., Bildstein, O., Arnoux, P., et al. (2019). Experimental characterization of coupled diffusion reaction mechanisms in low permeability chalk. *Chemical Geology*, *503*, 29–39. https://doi.org/10.1016/j.chemgeo.2018.10.016

Rendón-Angeles, J., Matamoros-Veloza, Z., López-Cuevas, J., Pech-Canul, M., & Yanagisawa, K. (2008). Stability and direct conversion of mineral barite crystals in carbonated hydrothermal fluids. *Journal of Materials Science*, *43*(7), 2189–2197. https://doi.org/10.1007/s10853-007-2044-5

Reynolds, O. (1883). XXIX. An experimental investigation of the circumstances which determine whether the motion of water shall be direct or sinuous, and of the law of resistance in parallel channels. *Philosophical Transactions of the Royal Society of London*, *174*, 935–982. https://doi.org/10.1098/rstl.1883.0029

Robinson, R. A., & Stokes, R. H. (2002). Electrolyte solutions. *Courier Corporation*.

Robson, M. D., Gatehouse, P. D., Bydder, M., & Bydder, G. M. (2003). Magnetic resonance: An introduction to ultrashort TE (UTE) imaging. *Journal of Computer Assisted Tomography*, *27*(6), 825–846. https://doi.org/10.1097/00004728-200311000-00001

Schulz, R. (2020). Degenerate equations in a diffusion–precipitation model for clogging porous media. *European Journal of Applied Mathematics*, *31*(6), 1050–1069. https://doi.org/10.1017/S0956792519000391

Schulz, R., Ray, N., Frank, F., Mahato, H., & Knabner, P. (2017). Strong solvability up to clogging of an effective diffusion–precipitation model in an evolving porous medium. *European Journal of Applied Mathematics*, *28*(2), 179–207. https://doi.org/10.1017/S0956792516000164

Seigneur, N., De Windt, L., Poyet, S., Socié, A., & Dauzeres, A. (2022). Modelling of the evolving contributions of gas transport, cracks and chemical kinetics during atmospheric carbonation of hydrated C3S and CSH pastes. *Cement and Concrete Research*, *160*, 106906. https://doi.org/10.1016/j.cemconres.2022.106906

Seigneur, N., Mayer, K. U., & Steefel, C. I. (2019). Reactive transport in evolving porous media. *Reviews in Mineralogy and Geochemistry*, *85*(1), 197–238. https://doi.org/10.2138/rmg.2019.85.7

Seigneur, N., Socié, A., & Mayer, K. U. (2023). A compositional global implicit approach for modeling coupled multicomponent reactive transport. *Water Resources Research*, *59*(5), e2021WR031774. https://doi.org/10.1029/2021WR031774

Sin, I., De Windt, L., Banc, C., Goblet, P., & Dequidt, D. (2023). Assessment of the oxygen reactivity in a gas storage facility by multiphase reactive transport modeling of field data for air injection into a sandstone reservoir in the Paris Basin, France. *Science of the Total Environment*, *869*, 161657. https://doi.org/10.1016/j.scitotenv.2023.161657

Sin, I., Lagneau, V., De Windt, L., & Corvisier, J. (2017). 2D simulation of natural gas reservoir by two-phase multicomponent reactive flow and transport—Description of a benchmarking exercise. *Mathematics and Computers in Simulation*, *137*, 431–447. https://doi.org/10.1016/j.matcom.2016.12.003

Soulaine, C. (2024). Micro-continuum modeling: An hybrid-scale approach for solving coupled processes in porous media. *Water Resources Research*, *60*(2), e2023WR035908. https://doi.org/10.1029/2023WR035908

Soulaine, C., Roman, S., Kovscek, A., & Tchelepi, H. A. (2017). Mineral dissolution and wormholing from a pore-scale perspective. *Journal of Fluid Mechanics*, *827*, 457–483. https://doi.org/10.1017/jfm.2017.499

Soulaine, C., Roman, S., Kovscek, A., & Tchelepi, H. A. (2018). Pore-scale modelling of multiphase reactive flow: Application to mineral dissolution with production of CO_2. *Journal of Fluid Mechanics*, *855*, 616–645. https://doi.org/10.1017/jfm.2018.655

Steefel, C. I. (2019). Reactive transport at the crossroads. *Reviews in Mineralogy and Geochemistry*, *85*(1), 1–26. https://doi.org/10.2138/rmg.2019.85.1

Steefel, C. I., & Hu, M. (2022). Reactive transport modeling of mineral precipitation and carbon trapping in discrete fracture networks. *Water Resources Research*, *58*(9), e2022WR032321. https://doi.org/10.1029/2022WR032321

Steefel, C. I., & Yang, L. (2021). Secondary magnesite formation from forsterite under CO_2 sequestration conditions via coupled heterogeneous nucleation and crystal growth. *Geochimica et Cosmochimica Acta*, *311*, 29–42. https://doi.org/10.1016/j.gca.2021.07.030

Steinwinder, J., & Beckingham, L. E. (2019). Role of pore and pore-throat distributions in controlling permeability in heterogeneous mineral dissolution and precipitation scenarios. *Water Resources Research*, *55*(7), 5502–5517. https://doi.org/10.1029/2019WR024793

Tartakovsky, A. M., Meakin, P., Scheibe, T. D., & Wood, B. D. (2007). A smoothed particle hydrodynamics model for reactive transport and mineral precipitation in porous and fractured porous media. *Water Resources Research*, *43*(5), 5437. https://doi.org/10.1029/2005WR004770

Tartakovsky, A. M., Redden, G., Lichtner, P. C., Scheibe, T. D., & Meakin, P. (2008). Mixing-induced precipitation: Experimental study and multiscale numerical analysis. *Water Resources Research*, *44*(6), 6–10. https://doi.org/10.1029/2006WR005725

Van Genuchten, M. T. (1980). A closed-form equation for predicting the hydraulic conductivity of unsaturated soils. *Soil Science Society of America Journal*, *44*(5), 892–898. https://doi.org/10.2136/sssaj1980.03615995004400050002x

Vehling, F., & Shao, H. (2023). Two-phase reactive transport modeling of heterogeneous gas production in a low-and intermediate-level waste repository. *Safety of Nuclear Waste Disposal*, *2*, 128–129. https://doi.org/10.1016/j.apgeochem.2024.106219

Wegner, L., Pohlmeier, A., Wang, Y., Klinkenberg, M., Bosbach, D., & Poonoosamy, J. (2024). Experimental data for: Investigating coupled mineral dissolution and precipitation processes with gas production in porous media using magnetic resonance imaging [Dataset]. *Jülich DATA*. https://doi.org/10.26165/JUELICH-DATA/OBASAC

Xu, R., Li, R., Ma, J., He, D., & Jiang, P. (2017). Effect of mineral dissolution/precipitation and CO_2 exsolution on CO_2 transport in geological carbon storage. *Accounts of Chemical Research*, *50*(9), 2056–2066. https://doi.org/10.1021/acs.accounts.6b00651

Xu, T., Spycher, N., Sonnenthal, E., Zhang, G., Zheng, L., & Pruess, K. (2011). Toughreact version 2.0: A simulator for subsurface reactive transport under non-isothermal multiphase flow conditions. *Computers & Geosciences*, *37*(6), 763–774. https://doi.org/10.1016/j.cageo.2010.10.007

Yang, W., Chen, M. A., Lee, S. H., & Kang, P. K. (2024). Fluid inertia controls mineral precipitation and clogging in pore to network–scale flows. *Proceedings of the National Academy of Sciences*, *121*(28), e2401318121. https://doi.org/10.1073/pnas.2401318121

Zhou, C.-X., Hu, R., Deng, H., Ling, B., Yang, Z., & Chen, Y.-F. (2023). Surface-volume scaling controlled by dissolution regimes in a multiphase flow environment. *Geophysical Research Letters*, *50*(18), e2023GL104067. https://doi.org/10.1029/2023GL104067

References From the Supporting Information

Ahmed, T. (2009). *Working guide to reservoir rock properties and fluid flow*. Gulf Professional Publishing.